

Magnetic order and its interplay with structure phase transition in the van der Waals ferromagnet VI₃

Yiqing Hao^{1#}, Yiqing Gu^{1#}, Yimeng Gu¹, Erxi Feng², Huibo Cao², Songxue Chi², Hua Wu^{3,4} and Jun Zhao^{1,4,5*}

¹State Key Laboratory of Surface Physics and Department of Physics, Fudan University, Shanghai 200433, China

²Neutron Scattering Division, Oak Ridge National Laboratory, Oak Ridge, Tennessee 37831, USA

³Laboratory for Computational Physical Sciences (MOE), State Key Laboratory of Surface Physics and Department of Physics, Fudan University, Shanghai 200433, China

⁴Collaborative Innovation Center of Advanced Microstructures, Nanjing 210093, China

⁵Shanghai Qi Zhi Institute, Shanghai 200232, China

Van der Waals magnet VI₃ demonstrates intriguing magnetic properties that render it great for use in various applications. However, its microscopic magnetic structure has not been determined yet. Here, we report neutron diffraction and susceptibility measurements in VI₃ that reveal a ferromagnetic order with the moment direction tilted from the *c* axis by ~36 degrees at 4 K. A spin reorientation accompanied by a structure distortion within the honeycomb plane is observed, before the magnetic order completely disappears at $T_c=50$ K. The refined magnetic moment of $\sim 1.3 \mu_B$ at 4 K is significantly lower than the fully ordered spin moment of $2 \mu_B/V^{3+}$, suggesting the presence of a considerable orbital moment anti-parallel to the spin moment and strong spin-orbit coupling in VI₃. This results in strong magnetoelastic interactions that make the magnetic properties of VI₃ easily tuned via strain and pressure.

Elucidating the nature of magnetism in low dimensional materials is of great importance in fundamental and applied physics [1]. In recent years, the discovery of ferromagnetism in two-dimensional (2D) van der Waals materials down to the monolayer limit [2-4] has triggered tremendous research interest. The 2D nature of the van der Waals magnets enables their magnetism to be tuned by various external stimuli [2-13], showing great promise for application in spintronic devices [14-20]. In the intensively-studied 2D ferromagnetic semiconductor CrI₃, the spin degree of freedom dominates the magnetism, and hence becomes the main target of various tuning methods [2,5-12]. However, the orbital magnetism, which is often neglected in 3d transition metal materials, has not been paid sufficient attention. VI₃, a semiconducting van der Waals ferromagnet, has received significant attention only recently [21-30]. Although both CrI₃ and VI₃ belong to the family of transition metal trihalides, they have different electron configurations of magnetic ions ($3d^3$ for Cr³⁺, and $3d^2$ for V³⁺). While the orbital moment of Cr³⁺ is largely quenched in the octahedral crystal field, V³⁺ has 3-fold orbital degeneracy ($L = 1$), and therefore the orbital degree of freedom could play a more important role in VI₃ [31-34].

Experimental studies show that the lattice, magnetic and electronic structures of VI₃ [21-30] are much more complicated compared to CrI₃. In contrast to the trigonal low temperature phase observed in CrI₃ [35], VI₃ exhibits two-step structure phase transitions at $T_{s1} \sim 79$ K and $T_{s2} \sim 32$ K [21-25]. Different low-temperature lattice structures in VI₃ have been reported in different experiments, including trigonal (*R*-3) [21], monoclinic (*C*2/*c*) [23,24] and triclinic (*P*-1) [25] space groups. The V-V bonds lengths are thusly found in hexagon [21], anti-dimerization [24] and dimerization [25] for different structures, respectively. Meanwhile, while in CrI₃ the

magnetic moments are aligned along the c -axis throughout the whole ferromagnetic phase [35], there are experiments suggesting that the magnetization easy axis in VI_3 is deviated from the c axis [27,28]. The magnitude of magnetic moments is also controversial in different measurements, for instance the moments along the c -axis are found ranging from $0.95 \mu_B / \text{V}^{3+}$ to $2.47 \mu_B / \text{V}^{3+}$ [21,22,24,27-29]. Moreover, in contrast to the fully ordered ($\sim 3 \mu_B / \text{Cr}^{3+}$) CrI_3 [35], large orbital moment and strong spin-orbit coupling were proposed in VI_3 to explain the deviation of V^{3+} moment from classical estimation [31-34]. However, there have been contradicting opinions regarding the character of the orbital moments. Some authors suggested that the orbital moment is parallel to the spin moment [34] while others instead suggested they are antiparallel-aligned [31-33]. Alternately, it was also proposed that the twin orbital orders would result in zero orbital moments [36].

Here we use neutron diffraction and thermodynamic measurements to study the structural and magnetic ordering properties of VI_3 . Our polycrystalline samples were grown by the solid state reaction method. A stoichiometric mixture of vanadium powder and iodine grains was sealed in evacuated quartz tubes, which were flushed by Ar gas. The sealed quartz tubes were first heated to 120°C holding for 4 hours, and then annealed at 400°C for 2 days. The resulting powder was ground and placed in Ar atmosphere for 2 days. The VI_3 single crystals were grown by the chemical vapor transport method [24]. Single-crystal neutron diffraction experiments were performed on the HB-3A Four-Circle Diffractometer equipped with a 2D detector at the High Flux Isotope Reactor (HFIR), Oak Ridge National Laboratory (ORNL). Powder neutron diffraction experiment was carried out on the HB-3 Triple-Axis Spectrometer at HFIR, ORNL. 4.5 grams of VI_3 powder sample was loaded and sealed in an aluminum can in He glove box. Pyrolytic graphite filters were used to eliminate higher order neutrons. Temperature-dependent magnetic susceptibility and specific heat data were collected using Quantum Design DYNACOOOL system. Field-dependent magnetization measurements were performed using Quantum Design MPMS3 SQUID magnetometer.

VI_3 consists of vanadium honeycomb layers coupled via van der Waals interactions. The I ions are octahedrally coordinated around each V^{3+} ion (Fig. 1a). Field-dependent magnetization data of VI_3 at 2 K show clear ferromagnetic hysteresis in both the c -axis and ab -plane (Fig. 1b), contrary to neglectable coercivity in CrI_3 at the same temperature [35]. Temperature-dependent magnetization and specific heat data clearly show two transitions at $T_C = 50$ K and $T_{s1} = 79$ K (Fig. 1c,d), corresponding to the ferromagnetic transition and the structural phase transition, respectively.

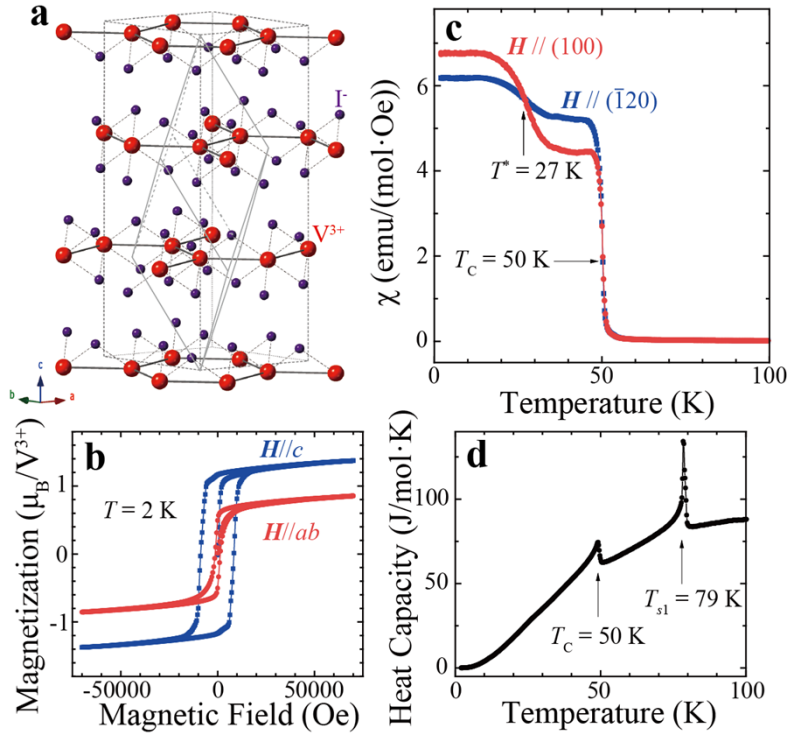


Fig. 1. (a) Crystal structure of VI_3 represented in trigonal lattice. The rhombohedral lattice is also drawn by solid and dashed gray lines in center. (b) Field-dependent magnetization in c -axis (blue) and ab -plane (red) at 2 K showing clear ferromagnetic hysteresis loops. (c) Temperature-dependent field-cooled magnetic susceptibilities. Magnetic field of $H = 200$ Oe were applied along hexagonal (100) (red) and its orthogonal direction within ab -plane (blue), T^* represents the proposed transition temperature of spin reorientation. (d) Temperature-dependent specific heat of VI_3 . Two peaks are found at $T_C = 50$ K and $T_{s1} = 79$ K.

In order to determine the lattice and magnetic structure, we first performed neutron powder diffraction (NPD) measurements on VI_3 polycrystalline samples. The results are summarized in Fig. 2, which illustrates the NPD patterns at 6 K, 40 K and 60 K. Figure 2 insets show the subtracted magnetic intensity at 6 K and 40 K to the paramagnetic state at 60 K, respectively. Clear magnetic Bragg peaks are observed at 6 K and 40 K at $\mathbf{Q} = (003)_h$, $(101)_h$, $(012)_h$ and $(104)_h$. Here lower index h denotes that the peaks are indexed to hexagonal notation of the room-temperature $R\bar{3}$ trigonal space group. The magnetic Bragg peaks are analyzed by Rietveld refinements. We find the magnetic intensities of both 40 K and 6 K are best fitted by a ferromagnetic structure where the magnetic easy axis is tilted from c -axis towards the ab -plane. At 40 K, the ab -plane moment is $0.50(3) \mu_B$ and the c -axis moment is $0.78(6) \mu_B$. At 6 K, the ab -plane moment is $0.69(2) \mu_B$ and the c -axis moment is $1.03(4) \mu_B$. Intriguingly, the angle between magnetic easy axis and honeycomb c -axis is nearly unchanged on cooling from 40 K to 6 K. This is different from CrI_3 where the Cr^{3+} moments are ferromagnetically aligned along c -axis.

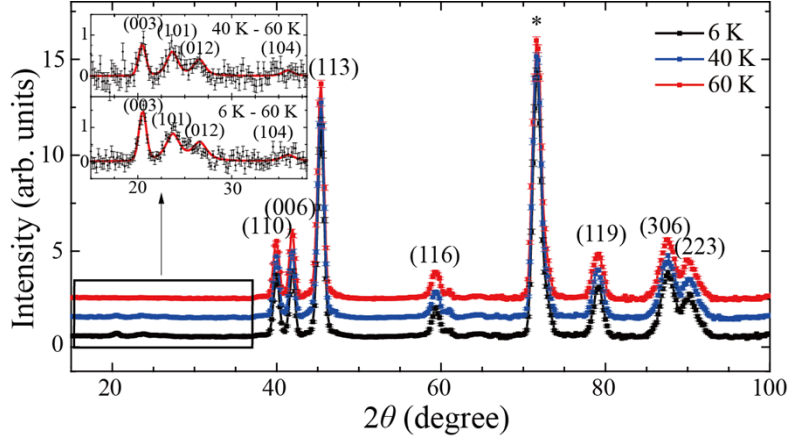


Fig. 2. Neutron power diffraction pattern of VI₃. The wavelength used is 2.359 Å. Black, blue, and red lines represent diffraction intensities measured at 6 K, 40 K and 60 K, respectively. Diffraction patterns for 40 K and 60 K are shifted in y -axis for clarity. The magnetic peaks and main nuclear Bragg peaks are indexed using hexagonal notation. The star denotes the background signal from aluminum sample can. Insets show the Rietveld refinements of the subtracted magnetic peaks at 40 K and 6 K using the magnetic structure described in the main text. The black dots and red lines represent observed and calculated intensities, respectively.

In our NPD refinements, intensities of the C_3 symmetric peaks are summed therefore the moment directions within the ab -plane is indistinguishable. To determine the moment directions within the ab -plane, we performed neutron diffraction measurements on high quality single-crystalline VI₃ at HB-3A Four-Circle Diffractometer. The results are illustrated in Figure 3. Figure 3a shows the longitudinal cuts of (300)_h peaks at 60 K. Clear difference of peak positions are observed in (300)_h and (030)_h peaks. This suggests the breaking of C_3 symmetry which is also reported by previous low-temperature X-ray diffractions [23-25]. Similar splitting in peak positions are also observed at (306)_h, (036)_h and (3-36)_h at 4 K (Fig. 3b). The lattice parameters are refined from fitting more than ten Bragg peaks along different directions at each temperature (Table I). We show that the V-V bonds are dimerized below T_s where the V-V bond length along one direction ((100)_h in the hexagonal/trigonal notation) are shortened by ~1% than the other two V-V bond lengths (Fig. 3g). The splitting of (300)_h peaks as well as dimerized V-V bond lengths are in agreement with recently reported SXRD measurements [25]. Magnetic peaks at (003)_h, (101)_h and (012)_h are measured at 4 K, 40 K and 60 K and are illustrated in Fig. 3c-e. Clear enhancement of above magnetic peaks is observed at 4 K and 40 K compared to 60 K, which is consistent with our powder measurements. Noted the residue intensity of (003)_h at 60 K is due to the $\lambda/2$ contamination of the strong Bragg peak of (006)_h. Temperature dependence of the (003)_h peak revealed a clear transition at T_C (Fig. 3f). Critical exponential fitting yields $T_C = 50.3(5)$ K and critical exponent $\beta = 0.19(2)$, which is consistent with our heat capacity measurements (Fig. 1d).

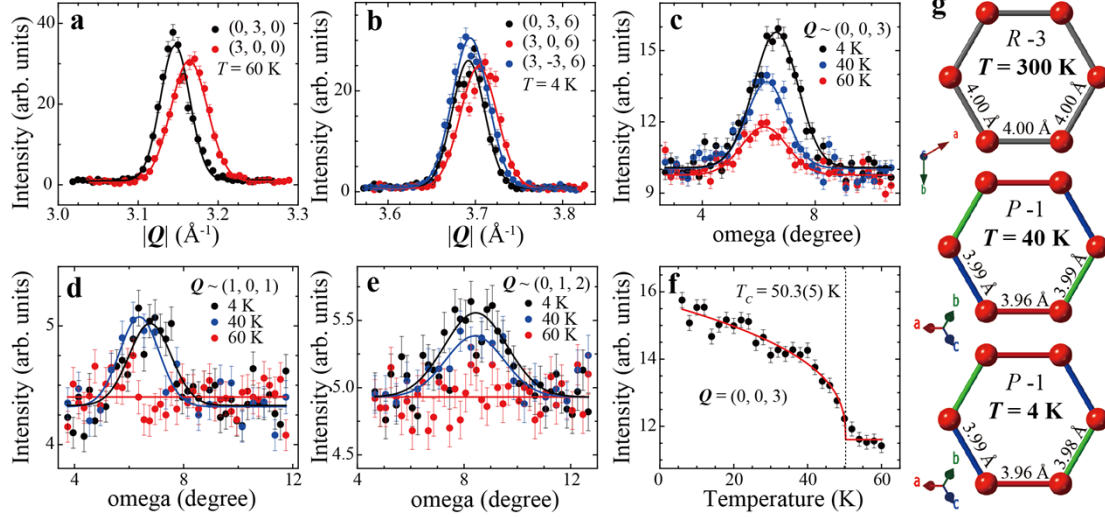


Fig. 3. Nuclear and magnetic Bragg peaks measured in single-crystalline VI_3 . The wavelength used is 1.542 \AA . (a) $(300)_h$ and $(030)_h$ measured at 60 K. (b) $(306)_h$, $(036)_h$ and $(3-36)_h$ measured at 4 K. Black, red and blue colors represent Bragg peaks along different in-plane directions. (c-e) $(003)_h$, $(101)_h$ and $(012)_h$ magnetic peaks measured at indicated temperatures. Solid lines are Gaussian fitting curves based on the magnetic structure refinements. (f) Temperature dependence of $(003)_h$ magnetic Bragg peak. The red line shows fitting using the critical exponential function. (g) V-V bond lengths at different temperatures. Red, blue and green color indicates three types of symmetric inequivalent V-V bonds below T_S . The arrows indicate the lattice directions in hexagonal (upper) and triclinic (middle and lower) notations, respectively.

We note that, while the intensity of $(003)_h$ increases drastically by cooling from 40 K and 4 K (Fig. 3c), the intensity of $(101)_h$ remains nearly unchanged (Fig. 3d). Such redistribution of peak intensities indicates the presence of a spin reorientation in the honeycomb ab -plane between 4 K and 40 K. Indeed, our refinements suggest that the magnetic moments at 4 K are $\mathbf{m}_\parallel = 0.84(5) \mu_B$ and $\mathbf{m}_c = 1.08(8) \mu_B$ with the in-plane moment parallel to the $(100)_h$ direction (Fig. 4a, c, e). At 40 K, the in-plane moment is rotated by 90° and perpendicular to $(100)_h$ (Fig. 4b, d, f). The magnitudes of the magnetic moments at 40 K are $\mathbf{m}_\perp = 0.51(5) \mu_B$, $\mathbf{m}_c = 0.65(6) \mu_B$. To further confirm the presence of the spin reorientation within the honeycomb ab -plane, we measured the temperature and angle dependence of the magnetization within the ab -plane (Fig. 1c). Below $T^* = 27 \text{ K}$, it is shown that the magnetization along $(100)_h$ is larger than that perpendicular to $(100)_h$, and the magnitude relation is reversed above T^* , as is expected for the spin reorientation transition revealed by our neutron diffraction experiment. This transition temperature T^* coincides with the $T_{\text{FM}} \approx 26 \text{ K}$ revealed by previous magnetization measurements [28,30]. Nevertheless, the angle of in-plane moment rotation is 90° by our single crystal refinement rather than 30° reported by previous angular dependent magnetization measurements [28].

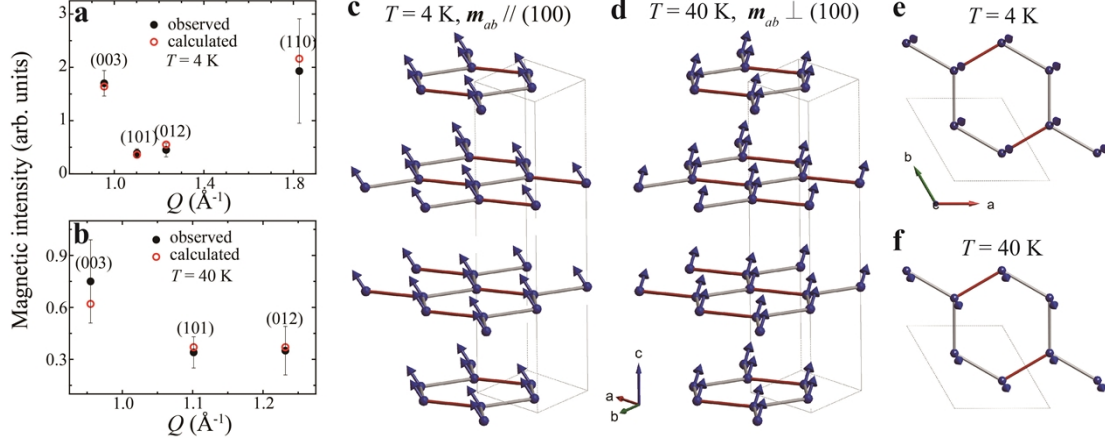


Fig. 4. (a-b) Magnetic structure refinement of VI_3 at 4 K and 40 K. Black dots and red circles represent observed and calculated magnetic peak intensities, respectively. (c-d) Magnetic structures of VI_3 at 4 K and 40 K. Blue arrows represent moment directions of V^{3+} and red bonds represent shortened V-V bonds.

From powder and single crystal neutron diffraction refinements, we estimate the ordered moment of VI_3 is $\sim 1.3(1) \mu_{\text{B}}/\text{V}^{3+}$. This value is much smaller than the classic estimation of pure spin moment of $2 \mu_{\text{B}}/\text{V}^{3+}$, in contrast to CrI_3 where the Cr^{3+} moments are fully ordered [35]. The reduced ordered moment in VI_3 can be understood by the unneglectable orbital moment aligned nearly antiparallel to the spin moment [31-33]. The spin-orbit coupling induces strong magnetic anisotropy, which may easily stabilize the magnetic order down to the monolayer limit. Meanwhile, the in-plane spin orientations of VI_3 strongly depend on local $[\text{VI}_6]$ octahedral environments therefore can be easily tuned by structural distortions. As a result, in-plane spin reorientation is observed at $T^* = 27$ K accompanied by a structural distortion within the honeycomb plane [23,25]. These results imply that VI_3 has great tunability of magnetism via strain, pressure and proximity effects, which calls for further exploration especially in its few-layer form.

In summary, we have shown by neutron diffraction and susceptibility measurements that the ferromagnetic moment of van der Waals magnet VI_3 is tilted by $\theta \sim 36^\circ$ from the c axis at 4 K. On warming to ~ 27 K, the in-plane moments rotate by 90 degrees from parallel to perpendicular to the $(100)_h$ direction, which is accompanied by the shrinkage of the V-V bond distance. The magnetic moments are about $0.93(8) \mu_{\text{B}}$ at 40 K and $1.24(5) \mu_{\text{B}}$ at 6 K, which are much lower than the fully order spin moment of V^{3+} . The moment reduction as well as magnetoelastic coupling can be understood by considering the presence of a considerable orbital moment and strong spin-orbit coupling, which in turns result in strong magnetoelastic interactions and is useful in designing highly-tunable spintronic devices in 2D limit.

This work was partially supported by the National Key R&D Program of the MOST of China (Grant No. 2016YFA0300203), the Innovation Program of Shanghai Municipal Education Commission (Grant No. 2017-01-07-00-07-E00018), the Shanghai Municipal Science and Technology Major Project (Grant No. 2019SHZDZX01), and the National Natural Science Foundation of China (Grant No. 11874119). E.F. and H.C. acknowledge the support of U.S. DOE

BES Early Career Award No. KC0402020 under Contract No. DE-AC05-00OR22725. This research used resources at the High Flux Isotope Reactor, a DOE Office of Science User Facility operated by the Oak Ridge National Laboratory.

	60K	40K	4K
a	7.685(11)	7.676(8)	7.674(11)
b	7.702(11)	7.699(11)	7.699(14)
c	7.711(11)	7.706(11)	7.695(19)
α	53.46(10)	53.44(10)	53.33(15)
β	53.11(10)	53.12(10)	53.07(14)
γ	53.22(9)	53.20(9)	53.22(11)
V-V(1)	3.967(7)	3.964(7)	3.963(9)
V-V(2)	3.991(10)	3.989(10)	3.977(15)
V-V(3)	3.996(8)	3.992(8)	3.988(10)

Table I. Lattice parameters and V-V bond lengths calculated from single crystal diffraction. The space group is $P -1$ (No. 2). The lattice axes are set based on room temperature rhombohedral lattice coordinates shown in figure 1a.

- [1] K. S. Burch, D. Mandrus, and J. G. Park, *Nature* **563**, 47 (2018).
- [2] B. Huang *et al.*, *Nature* **546**, 270 (2017).
- [3] C. Gong *et al.*, *Nature* **546**, 265 (2017).
- [4] Y. Deng *et al.*, *Nature* **563**, 94 (2018).
- [5] D. Zhong *et al.*, *Sci. Adv.* **3**, e1603113 (2017).
- [6] B. Huang *et al.*, *Nat. Nanotechnol.* **13**, 544 (2018).
- [7] S. Jiang, J. Shan, and K. F. Mak, *Nature Materials* **17**, 406 (2018).
- [8] S. Jiang, L. Li, Z. Wang, K. F. Mak, and J. Shan, *Nat. Nanotechnol.* **13**, 549 (2018).
- [9] W. Chen, Z. Sun, Z. Wang, L. Gu, X. Xu, S. Wu, and C. Gao, *Science* **366**, 983 (2019).
- [10] T. Li *et al.*, *Nature Materials* **18**, 1303 (2019).
- [11] T. Song *et al.*, *Nature Materials* **18**, 1298 (2019).
- [12] Z. Sun *et al.*, *Nature* **572**, 497 (2019).
- [13] L. Liu, K. Yang, G. Wang, and H. Wu, *Journal of Materials Chemistry C* **8**, 14782 (2020).
- [14] K. F. Mak, J. Shan, and D. C. Ralph, *Nat. Rev. Phys.* **1**, 646 (2019).
- [15] M. Gibertini, M. Koperski, A. F. Morpurgo, and K. S. Novoselov, *Nat. Nanotechnol.* **14**, 408 (2019).
- [16] C. Gong and X. Zhang, *Science* **363**, eaav4450 (2019).
- [17] W. Zhang, P. K. J. Wong, R. Zhu, and A. T. S. Wee, *InfoMat.* **1**, 479 (2019).
- [18] B. Huang, M. A. McGuire, A. F. May, D. Xiao, P. Jarillo-Herrero, and X. Xu, *Nature Materials* **19**, 1276 (2020).
- [19] V. P. Ningrum *et al.*, *Research (Washington, D.C.)* **2020**, 1768918 (2020).
- [20] S. Yang, T. Zhang, and C. Jiang, *Adv. Sci. (Weinh.)* **8**, 2002488 (2021).
- [21] S. Tian, J. F. Zhang, C. Li, T. Ying, S. Li, X. Zhang, K. Liu, and H. Lei, *J. Am. Chem. Soc.* **141**, 5326 (2019).

- [22] T. Kong, K. Stolze, E. I. Timmons, J. Tao, D. R. Ni, S. Guo, Z. Yang, R. Prozorov, and R. J. Cava, *Advanced Materials* **31**, 1808074 (2019).
- [23] P. Doležal *et al.*, *Physical Review Materials* **3**, 121401 (2019).
- [24] S. Son *et al.*, *Physical Review B* **99**, 041402 (2019).
- [25] T. Marchandier, N. Dubouis, F. Fauth, M. Avdeev, A. Grimaud, J.-M. Tarascon, and G. Rousse, arXiv:2104.00457 (2021).
- [26] E. Gati, Y. Inagaki, T. Kong, R. J. Cava, Y. Furukawa, P. C. Canfield, and S. L. Bud'ko, *Physical Review B* **100**, 094408 (2019).
- [27] J. Yan *et al.*, *Physical Review B* **100**, 094402 (2019).
- [28] A. Koriki *et al.*, *Physical Review B* **103**, 174401 (2021).
- [29] Y. Liu, M. Abeykoon, and C. Petrovic, *Physical Review Research* **2**, 013013 (2020).
- [30] J. Valenta *et al.*, *Physical Review B* **103**, 054424 (2021).
- [31] K. Yang, F. Fan, H. Wang, D. I. Khomskii, and H. Wu, *Physical Review B* **101**, 100402(R) (2020).
- [32] G.-D. Zhao, X. Liu, T. Hu, F. Jia, Y. Cui, W. Wu, M.-H. Whangbo, and W. Ren, *Physical Review B* **103**, 014438 (2021).
- [33] L. M. Sandratskii and K. Carva, *Phys. Rev. B* **103**, 214451 (2021).
- [34] Z. Zhou, S. K. Pandey, and J. Feng, *Physical Review B* **103**, 035137 (2021).
- [35] M. A. McGuire, H. Dixit, V. R. Cooper, and B. C. Sales, *Chemistry of Materials* **27**, 612 (2015).
- [36] C. Huang, F. Wu, S. Yu, P. Jena, and E. Kan, *Phys Chem Chem Phys* **22**, 512 (2020).